metals

MDPI

Article

Microstructure and Wear Resistance of FeCrV15 Coatings by Laser Cladding

Zhiwei Bi and Tianqing Li *

School of Materials Science and Engineering, Jiangsu University, Zhenjiang 212013, China; zhiweibi_first@163.com

* Correspondence: litq@ujs.edu.cn

Abstract: Improving the surface performance and service life of 60Si2Mn steel is an important issue in agricultural machinery. A FeCrV15 coating layer may exhibit excellent performance in wear resistance. This research focuses on studying the microstructure and wear resistance of the FeCrV15 coating layer at various scanning speeds through laser cladding. Microstructure, phase distribution, surface hardness, and wear resistance of the coating layers are analyzed using X-ray diffraction (XRD), scanning electron microscopy (SEM), a microhardness tester, and laser confocal microscopy. The results indicate that the FeCrV15 alloy coating consists of γ-Fe, V_8C_7, and Cr_7C_3. The microhardness of the FeCrV15 coatings increases with the increase in the scanning speed. At a scanning speed of 8 mm/s, the highest microhardness reaches 727.5 ± 27 HV, approximately 2.5 times higher than the substrate. The friction and wear test of the coating is conducted using a 4 mm diameter Si_3N_4 ball grinding pair. The coatings prepared at different scanning speeds exhibit lower average coefficients of friction and wear rates compared to the substrate. Both the average coefficient of friction and wear rate decrease with increasing scanning speed. At a scanning speed of 8 mm/s, the lowest average coefficient of friction and the lowest wear rate were observed. The main wear mechanisms of the coating are oxidative wear and adhesive wear, with a small amount of abrasive wear.

Keywords: laser cladding; FeCrV15; microstructure; wear resistance

Citation: Bi, Z.; Li, T. Microstructure and Wear Resistance of FeCrV15 Coatings by Laser Cladding. *Metals* **2024**, *14*, 1136. https://doi.org/10.3390/met14101136

Academic Editor: Roy Johnsen

Received: 11 September 2024
Revised: 3 October 2024
Accepted: 4 October 2024
Published: 5 October 2024

1. Introduction

Wear is a key factor that significantly impacts the long-term efficiency and reliability of agricultural machinery [1]. 60Si2Mn is widely recognized in the industry for its strength, excellent hardenability, high load-bearing capacity, and affordability. The rotary tiller blades in agricultural machinery, such as rotary tillers, are often made from 60Si2Mn, and their prolonged exposure to abrasive media (such as stones, soil, or other hard components) places higher demands on their wear resistance [2]. However, the low hardness, poor friction, and wear performance of 60Si2Mn lead to reduced reliability in harsh environments [3]. Therefore, enhancing the surface properties of 60Si2Mn is of great significance. Currently, several technologies are available to improve the surface properties of agricultural machinery, including plasma spraying [4], physical vapor deposition (PVD) [5], resurfacing welding [6], carburizing [7], nitriding [8], and laser cladding technology. Laser cladding (LC) is an advanced surface modification technique that utilizes high-energy laser beams to melt cladding materials and solidify them on the surface of the substrate and forms a cladding coating with high service performance [9]. Compared to other surface strengthening technologies, laser cladding offers several advantages [10,11]. It can enhance the comprehensive properties of materials' surfaces while preserving the original characteristics of the substrate [12,13]. In recent years, many scholars have demonstrated that using additive manufacturing technology to prepare coatings is a feasible and reliable method to improve materials' surface hardness and wear resistance. Bartkowski et al. [14] employed laser cladding technology to deposit Stellite-6/WC composite powder onto a

B27 substrate. It was demonstrated that the hard phases within the composite coating, such as WC, W_2C, M_7C_3, and $M_{23}C_6$, enhanced the wear resistance of the coating. Moreover, the composite coating presented a 25% lower wear rate compared to the substrate. Iron-based alloy materials, due to their close composition with the substrate, can easily form strong metallurgical bonds with the substrate. They also offer low cost, high hardness, and good wear resistance, making them highly promising for improving the wear and corrosion resistance of agricultural machinery. Hou et al. [15] successfully developed an innovative coating on 3Cr13 stainless steel using laser cladding with Fe-Cr-Mo-Co-C-B amorphous alloy powder. The maximum hardness achieved by the coating was 1179 $HV_{0.5}$, significantly higher than the 3Cr13 stainless steel substrate, which has a hardness of 200 $HV_{0.5}$, indicating a sixfold increase. During friction and wear tests conducted using a silicon nitride (Si_3N_4), the cladding coating demonstrated a substantial improvement in wear resistance, exhibiting a lower coefficient of friction and significantly reduced mass loss compared to the substrate. Lu et al. [16] used laser cladding technology to prepare Fe-based coatings. Their research found that a large amount of carbides ($M_{23}C_6$, M_7C_3) and chromides were distributed in the eutectic region between the dendrites in the coating. The hard phase CrB inhibited grain growth and promoted heterogeneous nucleation, resulting in finer and denser crystal structures and a more stable wear process with a lower wear rate. Basiru et al. [17,18] observed that adding Cr_3C_2 and VC enhancers to iron-based coatings significantly improved the wear and corrosion resistance of tools under harsh and abrasive impact conditions. FeCrV15 powder is a kind of iron-based powder containing Cr element. If the FeCrV15 powder is used as coating materials in laser cladding, the FeCrV15 coating layer may exhibit excellent performance in wear resistance. However, there are very a few public reports and articles involving the topic about FeCrV15 laser cladding layer on the steel 60Si2Mn surface.

Therefore, this paper will study the microstructure and wear resistance of FeCrV15 at different scanning speeds. What is the wear resistance performance of the FeCrV15 coating layer? And how does scanning speed affect the phase distribution? To address these objectives, the following work will be undertaken: A laser cladding platform will be developed and constructed. Subsequently, optimal laser cladding parameters will be identified, followed by experimental procedures to fabricate the FeCrV15 cladding layer. Comprehensive testing and analysis will then be conducted to evaluate the microstructure, phase composition, surface hardness, and wear resistance of the resulting coatings. Moreover, the influence of scanning speed on the phase composition and mechanical properties of the coatings will be thoroughly examined. This study will enrich the theoretical foundation of laser cladding with FeCrV15 and provide practical guidance for improving the coating process of FeCrV15 on 60Si2Mn steel, potentially leading to enhanced industrial applications of this material.

2. Materials and Methods

2.1. Materials

The hot-rolled 60Si2Mn was selected as the experimental substrate, with size of 100 mm × 50 mm × 12 mm. The chemical composition of 60Si2Mn steel is shown in Table 1. The surface of the substrate was ground with different grades of sandpaper (from 80# to 800#) to remove impurities, followed by cleaning with anhydrous ethanol and acetone. X-FeCrV15 V2 (53–150 μm) Fe-based alloy powder produced by Höganäs Company (Helsingborg, Sweden) was chosen as the coating materials. The chemical composition of X-FeCrV15 V2 is shown in Table 2. Before laser cladding, the alloy powder was dried in a vacuum oven at of 100 °C for 3 h.

Table 1. Nominal chemical composition of 60Si2Mn (wt.%).

Component	C	Si	Mn	P	S	Cr	Ni	Cu	Fe
60Si2Mn	0.56~0.64	1.5~2.0	0.7~1.0	≤0.035	≤0.035	≤0.035	≤0.035	≤0.025	Bal.

Table 2. Nominal chemical composition of X-FeCrV15 V2 (53–150 μm) (wt.%).

Component	C	Mo	Mn	Cr	Si	V	Fe
X-FeCrV15 V2	4.3	1.3	1.0	13.8	1.0	15.1	Bal.

2.2. Laser Cladding System

The equipment utilized in this study was an integrated system (shown in Figure 1), primarily composed of a laser device (TruDisk 6002, Trumpf Company, Ditzingen, Germany), a robot (H60A, KUKA AG, Augsburg, Germany), a laser cladding head, an air compressor, a shielding gas system, and a water-cooling system. The laser device has a maximum output power of 6000 W, with a wavelength of 1030 nm. The 200 μm core diameter fiber is used to transmit the laser energy from the TruDisk 6002 to the cladding head. The defocusing amount was 0 mm to ensure the coincidence of the deposition plane and the laser focal plane and to improve the laser energy and powder capture efficiency. Argon (Ar), with a purity of 99.99%, was employed as the shielding gas, with a flow rate of 10 L/min. The preplacement was performed by evenly spreading the FeCrV15 powder on the surface of the substrate steel plate, controlling the preset layer thickness at 1.5 mm using a mold. Excess powder was removed with a glass rod. The powder was then compacted by 90–100 kg load for about 5 min. The laser power and scanning speed were designed based on preliminary experiments, and the experimental parameters selected for this study are shown in Table 3.

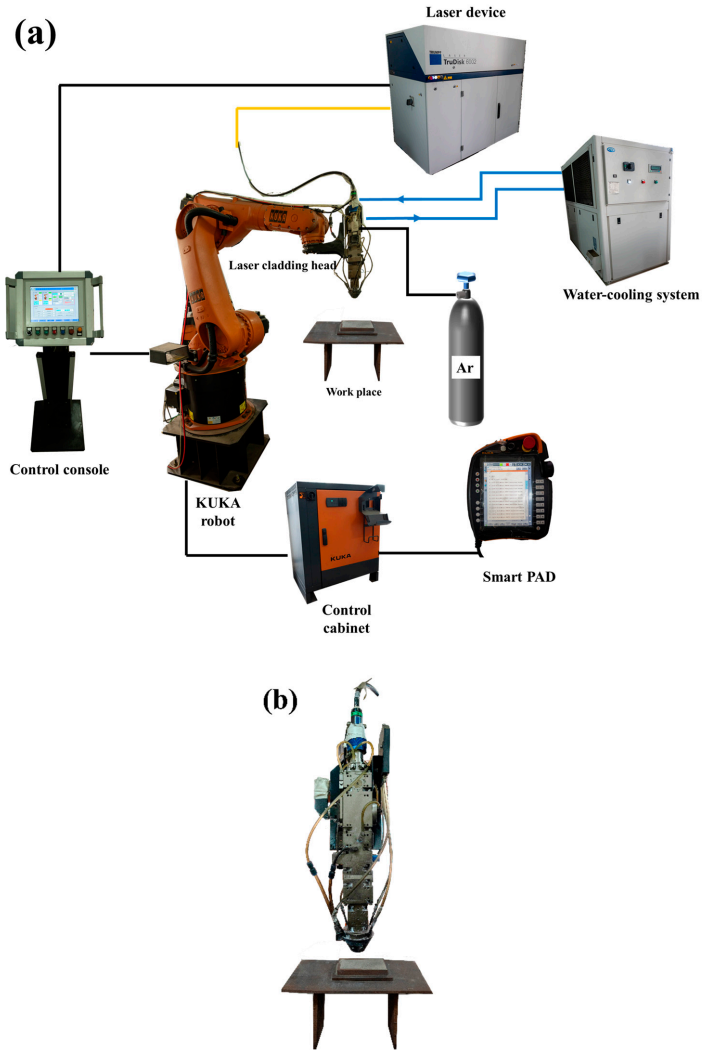

Figure 1. (**a**) Laser cladding system, (**b**) diagram of laser cladding.

Table 3. Experimental parameter table.

Samples	Substrate Material	Powder Used	Laser Beam Power (W)	Scanning Speed (mm/s)
1	60Si2Mn	X-FeCrV15 V2	1600	4
2				6
3				8

2.3. Specimen Preparation and Detection after Laser Cladding

A metallographic sample was taken perpendicular to the laser movement direction, and #60, #120, #240, #600, #1000, #1200, #1500, and #2000 mesh round metallographic dry sandpapers were placed on a metallographic sample grinding and polishing machine for fine grinding and polishing of the coating samples. The etching solution was composed of $FeCl_3$ (1 g), HCl (3 mL), and H_2O (20 mL). Etching was performed at room temperature, with the cross-section immersed for 30–60 s, depending on the reaction rate with the material. The sample was then immediately rinsed with distilled water and alcohol to stop the etching process. After etching, the sample was dried to prevent oxidation or further corrosion. The etched cross-section's microstructure was examined using a field emission scanning electron microscope (SEM, NovaNamo450, FEI Company, Hillsboro, OR, USA). The coating's phase composition was identified by an X-ray diffractometer (XRD, SmartLab, Rigaku Corporation, Tokyo, Japan) with a scanning range of 10° to 100° 2θ and a scanning speed of 5°/min.

The longitudinal cross-sectional hardness at different distances from the surface of the cladding coating was measured using a fully automatic microhardness tester (FM-ARS900, Future-Tech, Tokyo, Japan). The measurement point intervals were set at 100 μm, with a load of 300 gf and a dwell time of 15 s. Each test was averaged three times over the same area to reduce errors.

Before the wear experiment, #60, #120, #240, #600, #1000, #1200, #1500, and #2000 mesh round metallographic dry sandpapers were used on a metallographic sample grinding and polishing machine for fine grinding and polishing of the substrate and coating samples, ensuring that the roughness average (Ra) < 0.2 μm. The room temperature wear resistance of the coating was evaluated using a high-temperature friction and wear tester (HT-1000, Zhongke Kaihua Technolog Company, Lanzhou, China). The test used a 4 mm diameter Si_3N_4 ball grinding pair under the following conditions: constant temperature of 20 °C, applied load of 10 N, rotation speed of 200 r/min, and a duration of 30 min. After each test, a new Si_3N_4 ball grinding pair was used. A laser confocal microscope (OLS4100, Olympus Corporation, Tokyo, Japan) was used to measure the depth and width of the wear track to determine the wear rate of the coatings prepared with different parameters. Each specimen was tested three times to reduce errors. SEM was used to observe the wear morphology of the tested samples and analyze the wear mechanism.

The wear rate (W) is an important indicator of a material's wear resistance and can be calculated using the following formula:

$$W = \frac{V}{FL} \tag{1}$$

In the equation, V represents the wear volume (mm^3), F is the applied load (N), and L is the total sliding distance (m).

3. Results and Discussion

3.1. The Characteristics of the Coatings and Its Microstructures

Figure 2 shows the microstructure of the FeCrV15 coating at different scanning speeds. As shown in the figure, the surface topography of the FeCrV15 coating generally demonstrates good formation quality. Additionally, it presents three typical morphological characteristics: the bonding zone between the cladding coating and the substrate, which exhibits

characteristics of rapid solidification; the microstructure near the bonding zone of the cladding coating, consisting of dendritic grains (including some cellular grains); and the equiaxed grains at the surface end of the cladding coating. The changes in the crystallization morphology in the surface metallurgical coating are mainly controlled by the G/V ratio (G representing the temperature gradient and V representing the crystallization velocity). At the interface between the cladding coating and the substrate, the temperature gradient is the largest, but the crystallization rate in the molten pool is the slowest. As a result, the metal in the molten pool grows in a planar manner, forming a very thin planar grain zone. As the liquid–solid interface moves, the temperature gradient in the molten pool gradually decreases, while the crystallization rate gradually increases, leading to the formation of cellular grains. In the liquid phase ahead of the crystallization zone, compositional undercooling occurs, causing the crystallization morphology to change from cellular to dendritic grains, with some dendritic grains showing preferential growth and the presence of directionally solidified columnar dendritic structures. As the liquid–solid interface continues to advance, the temperature gradient in the liquid phase continues to decrease, and the crystallization rate becomes faster, causing the dendritic grains to become progressively finer. At the top of the molten pool, the heat dissipation conditions change because heat can be dissipated through the substrate by conduction and through the surrounding air medium by radiation and convection. At this time, the compositional undercooling in the molten pool is significant, placing the molten pool in a deeply undercooled state and increasing the nucleation rate. This results in finer crystallization grains and an equiaxed grain structure.

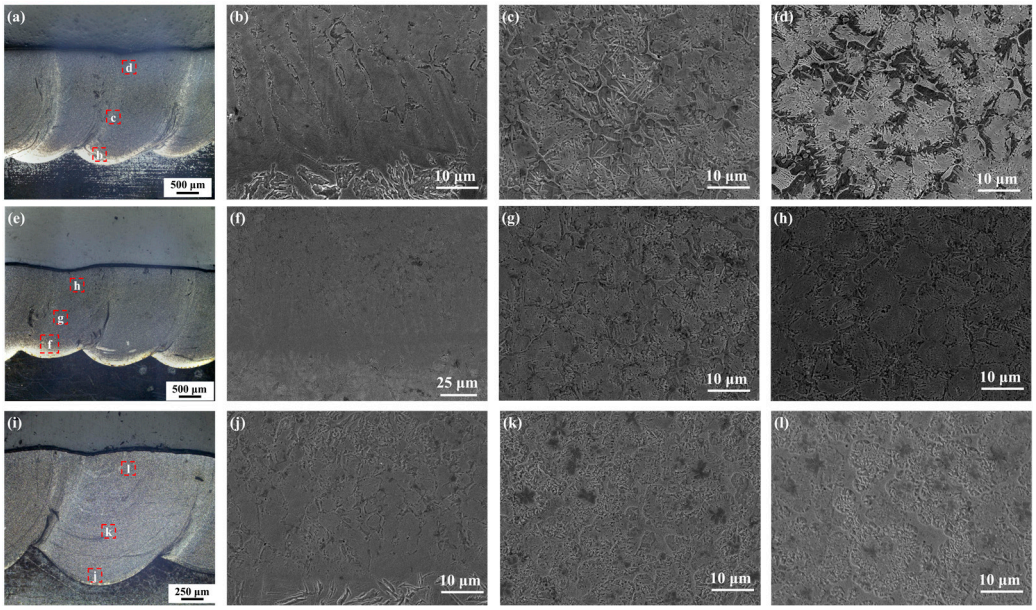

Figure 2. Microstructure of the laser cladding coatings at different scanning speeds: (**a**–**d**) 4 mm/s: cross-sectional morphology, combining area, central section, and top of the cladding coating; (**e**–**h**) 6 mm/s: cross-sectional morphology, combining area, central section, and top of the cladding coating; (**i**–**l**) 8 mm/s: cross-sectional morphology, combining area, central section, and top of the cladding coating.

The composition of different areas of the coating was determined using energy-dispersive spectroscopy (EDS). The analysis locations and results are shown in Figure 3 and Table 4. The results indicate that the coating mainly consists of dendrites, interdendritic eutectics, and dispersed intermetallic compounds. Point A represents the dendritic arms, point B represents the interdendritic gaps, and point C represents the dispersed intermetallic compounds.

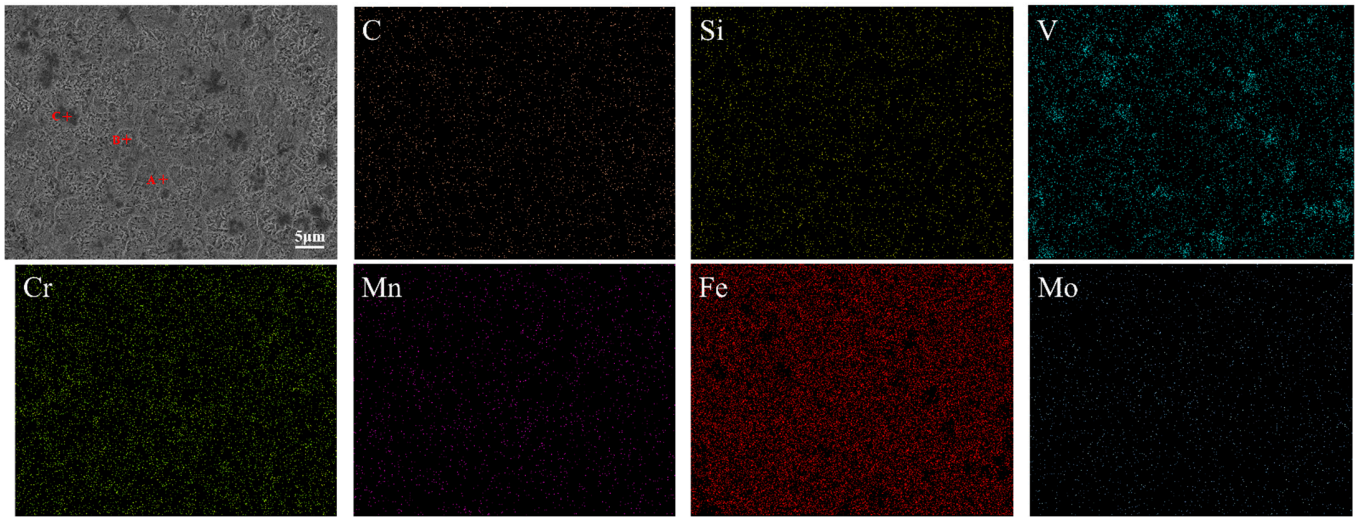

Figure 3. SEM image and EDS mapping scan of FeCrV15 coating.

Table 4. Chemical compositions of points A~C (%, atom fraction).

Point	C	Si	V	Cr	Mn	Fe	Mo	Possible Phase
A	20.80	0.70	4.31	16.08	0.01	57.75	0.26	Cr_7C_3
B	14.66	2.35	3.42	6.95	0.41	72.10	0.11	γ-Fe
C	34.58	0.13	48.45	2.42	0.04	14.18	0.20	V_8C_7

The FeCrV15 powder contains alloying elements such as C, Si, V, Cr, Mn, and Mo. Among these, C and Mn are austenite-forming elements, while Cr, Mo, V, and Si are ferrite-forming elements that narrow the austenite region. During the solidification process, the segregation of alloying elements can lead to differences in the microstructure. The EDS results show that the primary elements in the dendritic area (point A) are Cr and C; the main element in the interdendritic gap area (point B) is Fe; and the primary elements in the dispersed intermetallic compound area (point C) are V and C.

Figure 4 presents the phase analysis results of the coating, which shows that the coating is mainly composed of γ-Fe, V_8C_7, and Cr_7C_3. Based on the EDS results and the XRD analysis, it can be inferred that the dendrites consist of Cr_7C_3, the interdendritic gap area is composed of the γ-Fe solid solution, and the dispersed intermetallic compounds in the dendrites consist of V_8C_7.

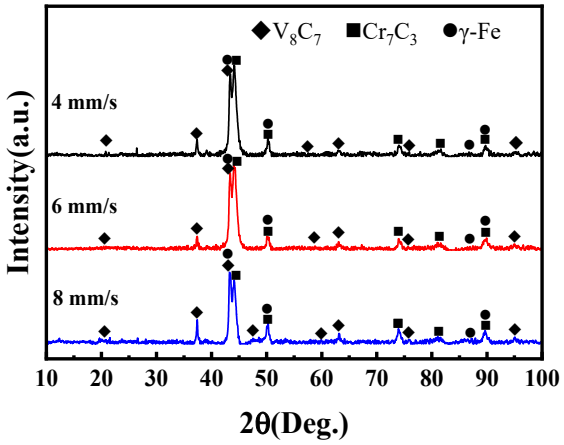

Figure 4. XRD analysis of coating.

The effects of scanning speed on microstructure of the FeCrV15 alloy coating are studied. Figure 5 shows coatings prepared at different scanning speeds by SEM. Black

dot-like V_8C_7 and a network-like structure of Cr_7C_3 and V_8C_7 attached to dendrites can be observed. The eutectic vanadium carbides precipitate at a temperature of approximately 1650 °C, and at temperatures below the separation line of vanadium carbides, Cr-rich carbides begin to form [6]. When the scanning speed is 8 mm/s, a large amount of reinforcement phases is produced. However, as the scanning speed decreases, the heat input increases, resulting in fewer reinforcement phases forming in the coating. This is because when the heat input is too high, the elements that form the reinforcement phases are burned off, leading to a reduction in the reinforcement phases.

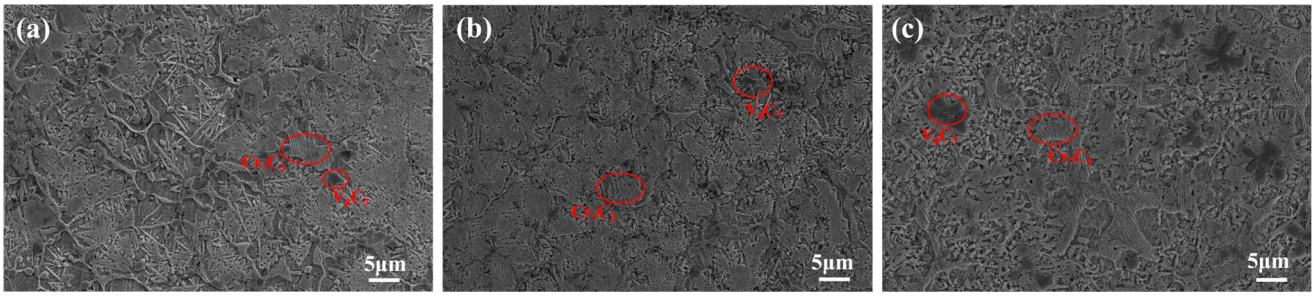

Figure 5. SEM images of coating at different scanning speeds (**a**) 4 mm/s, (**b**) 6 mm/s, (**c**) 8 mm/s.

3.2. The Microhardness of Coatings

The microhardness test results from the coating to the 60Si2Mn substrate are shown in Figure 6. As depicted in the figure, the microhardness values progressively increase from the substrate through the heat-affected zone to the coating. The hardness values of the coating are all higher than those of the substrate, and the hardness values in the heat-affected zone are intermediate between the substrate and the coating.

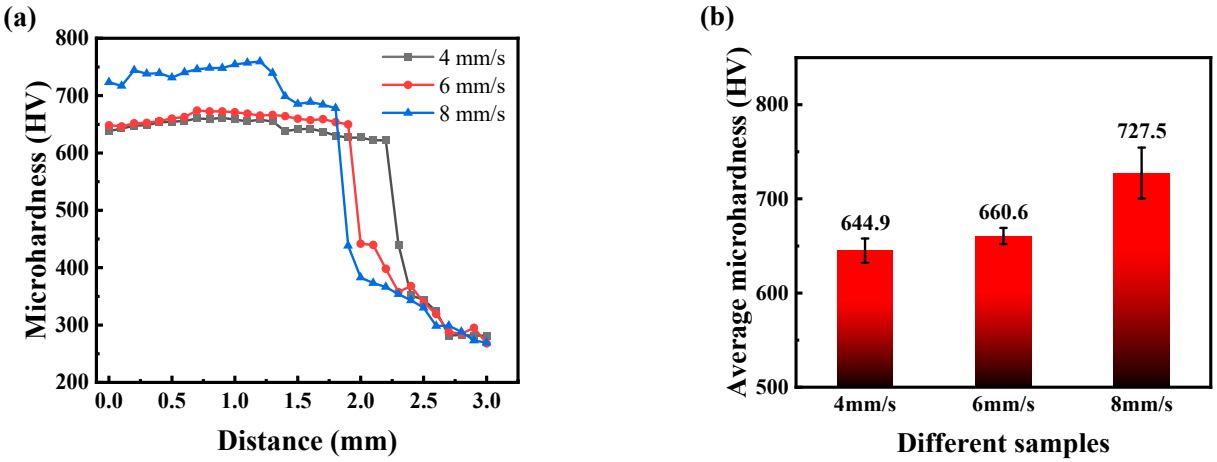

Figure 6. Microhardness of coating: (**a**) the hardness distribution from the surface to the substrate direction in the coating and (**b**) the average hardness of the coating area.

The increase in hardness can be attributed in part to the solid solution strengthening effect of the γ-Fe solid solution in the coating, and in part to the dispersion strengthening effect of V_8C_7 and Cr_7C_3 phases formed in the coating. Additionally, laser cladding is a welding process characterized by rapid melting and rapid cooling, resulting in fine-grained microstructures in the coating. This fine-grain strengthening effect leads to an increase in coating hardness.

The primary phase in the heat-affected zone is γ-Fe, and the content of hard phases is relatively low, leading to a decrease in hardness compared to the coating. The average hardness of the coating increases with increasing scanning speed, reaching an average maximum microhardness of 727.5 ± 27 HV at a scanning speed of 8 mm/s, approximately

2.5 times that of the 60Si2Mn substrate. The increase in hardness may be due to the rapid cooling rate, which generates greater mechanical stresses, leading to more dislocation entanglements.

3.3. Coefficient of Friction Analyzed

Figure 7a shows the friction coefficient curves of the FeCrV15 coating and 60Si2Mn. From the figure, the friction coefficients of both the 60Si2Mn substrate and FeCrV15 coating rise quickly in the initial stage and then tend to stabilize in the later stage. During the run-in phase, the friction coefficient of the 60Si2Mn substrate increases rapidly compared to the coating. This is because at the early stage of friction, the actual contact area between Si_3N_4 and the substrate is small, leading to higher contact stress, which results in a dramatic increase in the coefficient of friction. In contrast, the friction coefficient of the FeCrV15 coating rises more slowly, possibly due to debris generation, oxide formation, and the removal of the initial surface topography [19]. In the steady state friction phase, due to the transformation from point contact to surface contact, the contact stress decreases. The friction coefficients of both the 60Si2Mn substrate and FeCrV15 coating increase slowly, maintaining relative stability without significant fluctuations, eventually tending to stabilize.

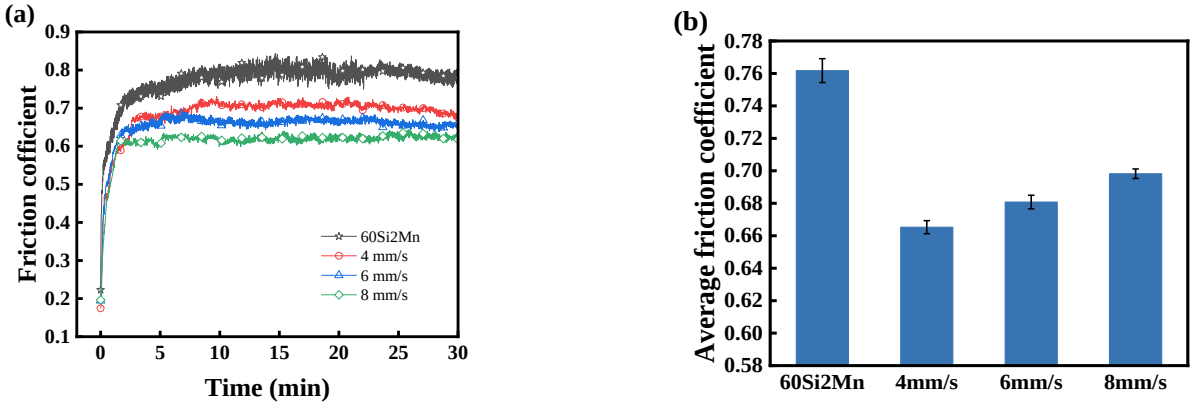

Figure 7. Friction coefficient analysis of FeCrV15 coatings and 60Si2Mn substrate: (**a**) friction coefficient change curve; (**b**) average coefficient of friction.

To observe the influence of different scanning speeds on the friction coefficient of the coating more clearly, the average friction coefficients of 60Si2Mn and FeCrV15 coatings at different scanning speeds were calculated, using the average results of three experiments for reliability, and plotted in Figure 7b. As shown in the figure, the average friction coefficient of the 60Si2Mn substrate is 0.76 ± 0.01, while the average friction coefficients of the coatings prepared at different scanning speeds are 0.68 ± 0.01, 0.65 ± 0.01, and 0.60 ± 0.01, respectively. The average friction coefficients of the coatings prepared at different scanning speeds are all lower than that of the substrate, and the average friction coefficient decreases as the scanning speed increases.

3.4. Wear Rate Analyzed

Figure 8 shows the three-dimensional morphology of wear marks on the 60Si2Mn substrate and FeCrV15 coatings. It can be observed that the wear on the 60Si2Mn substrate is the most severe, with wide and deep wear marks and pits, as well as furrows in the middle of the wear marks caused by the abrasion from Si_3N_4. In contrast, the wear marks on the edges and middle of the FeCrV15 coating are relatively shallow, and the surface of the FeCrV15 coating is smoother and more even than that of the 60Si2Mn substrate, with smaller furrows present.

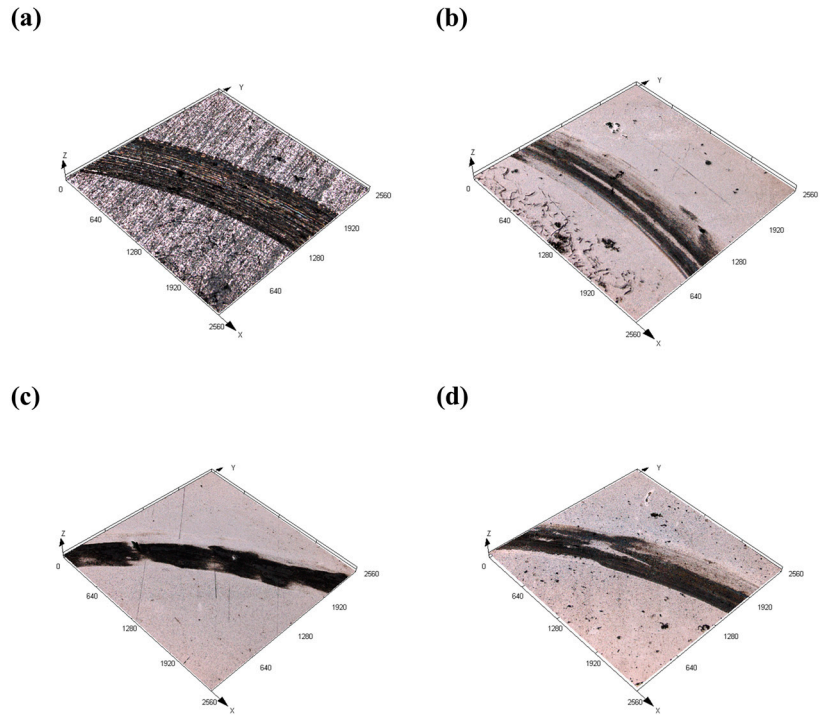

Figure 8. Three-dimensional morphology of wear marks on 60Si2Mn substrate and FeCrV15 coatings (**a**) 60Si2Mn (**b**) 4 mm/s, (**c**) 6 mm/s, (**d**) 8 mm/s.

Figure 9a shows the measurement results of the wear width and depth for the 60Si2Mn substrate and FeCrV15 coatings. For the measurements, different positions were selected, and the average of three sets of data was taken. The results show that the average wear width of the 60Si2Mn substrate is 983.57 ± 20 μm, and the average wear depth is 13.59 ± 1.50 μm. In comparison, the average wear widths of the FeCrV15 coating samples prepared at scanning speeds of 4 mm/s, 6 mm/s, and 8 mm/s are 689.72 ± 10 μm, 615.76 ± 4 μm, and 611.87 ± 50 μm, respectively, with average wear depths of 10.35 ± 1.00 μm, 6.50 ± 1.00 μm, and 5.30 ± 1.00 μm, respectively. The average wear width and depth of the FeCrV15 coatings are both lower than those of the 60Si2Mn substrate. The reduction in wear depth is due to the better wear resistance of the coating, making it more difficult for Si_3N_4 to wear down the coating. The significant variation in wear width may be attributed to the prolonged wear duration, during which the Si3N4 itself also experiences wear. The amount of wear on the Si_3N_4 differs depending on the coatings' wear resistance, which were prepared at different scanning speeds, resulting in the noticeable variation in wear width.

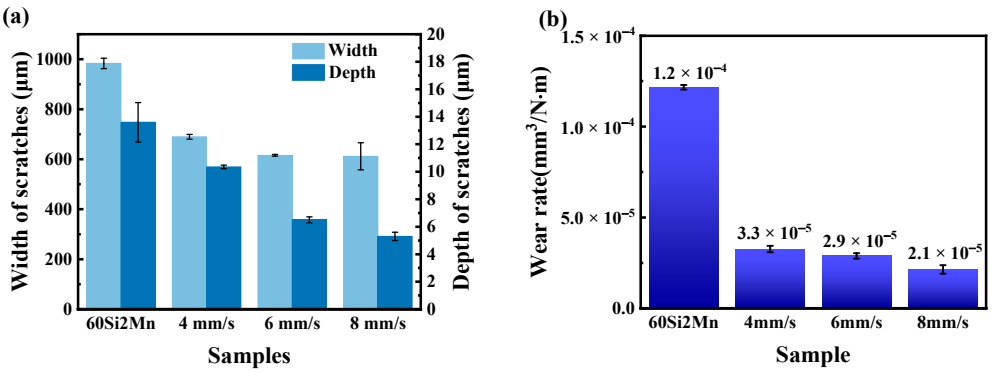

Figure 9. Wear characteristics of FeCrV15 coatings and 60Si2Mn substrate: (**a**) width and depth of wear marks; (**b**) wear rate.

Figure 9b shows the wear rates of the 60Si2Mn substrate and FeCrV15 coatings. The wear rate of the 60Si2Mn substrate is $1.2 \pm 0.02 \times 10^{-4}$ mm^3/N·m, while the wear rates of the coatings prepared at scanning speeds of 4 mm/s, 6 mm/s, and 8 mm/s are $3.3 \pm 0.2 \times 10^{-5}$ mm^3/N·m, $2.9 \pm 0.2 \times 10^{-5}$ mm^3/N·m, and $2.1 \pm 0.2 \times 10^{-5}$ mm^3/N·m, respectively. The wear rates of the FeCrV15 coatings are an order of magnitude lower than that of the substrate, indicating that the wear resistance of the coating is superior to that of the substrate. The coating prepared at a scanning speed of 8 mm/s exhibits the lowest wear rate, which is due to the formation of good metallurgical bonding between the coating and substrate, and the presence of a significant amount of high-hardness compound phases (V_8C_7, Cr_7C_3) in the coating contributing to dispersion strengthening. Moreover, the fine dendritic structure in the surface region of the coating improves the coating's toughness, reducing spalling during the wear process.

3.5. Wear Mechanism

Figure 10a shows the surface wear marks of the 60Si2Mn substrate, characterized by deep furrows, noticeable spalling, and cracking, indicating severe plastic deformation and damage during the wear test. EDS analysis shows that the adhesive material contains high levels of oxygen and silicon (O14.75, Si20.99), suggesting the presence of oxidative wear. Additionally, the Si element from the Si_3N_4 ball transferred to the substrate surface, indicating adhesive wear. Therefore, the main wear mechanisms of the substrate are adhesive wear and oxidative wear. In contrast, as shown in Figure 10b–d, the worn surface morphology of the cladding layer is relatively smooth, with only shallow furrows and small pores. During the wear test, due to the higher wear resistance of the coating, part of the Si_3N_4 counterpart is also worn down and evenly distributed in the wear marks. Throughout the wear process, the worn surface experiences oxidative wear, forming oxide and silicon films in the wear marks. As the wear progresses, a small number of hard phase particles (V_8C_7 and Cr_7C_3) may detach [20], forming small pores. The detached V_8C_7 and Cr_7C_3 particles slide along with the counterpart, wearing down the oxide and silicon films. The abrasive particles are pressed into the coating surface under normal load and are subsequently driven to cut the coating surface to create shallow furrows during the sliding process. In summary, the main wear mechanisms of the coating are oxidative wear and adhesive wear, with a small amount of abrasive wear.

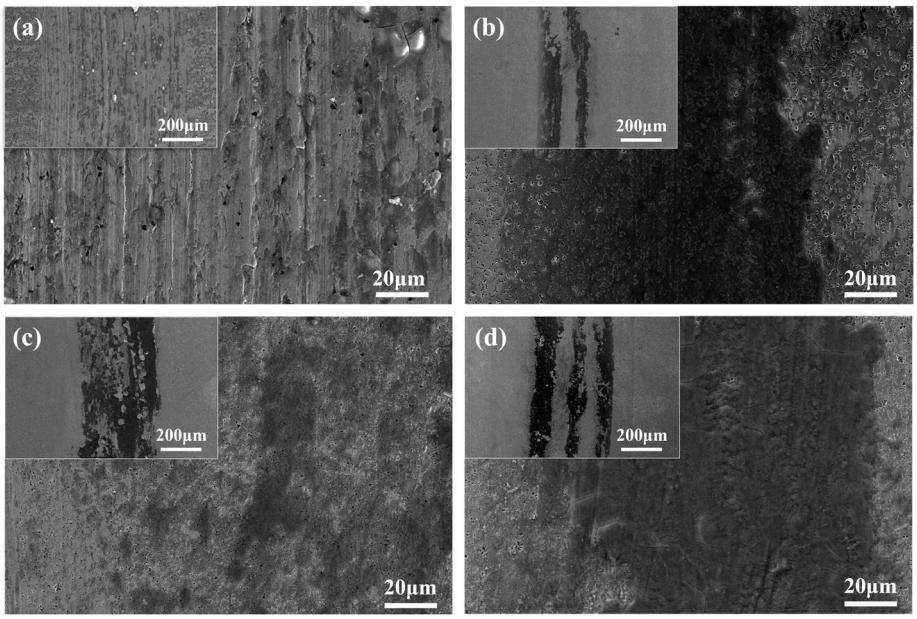

Figure 10. Wear morphology of 60Si2Mn and FeCrV15 cladding prepared by different scanning speeds: (**a**) 60Si2Mn (**b**) 4, (**c**) 6, and (**d**) 8 mm/s.

4. Conclusions

1. The FeCrV15 alloy coatings are prepared by laser cladding under different scanning speeds. There is a clear transition zone between 60Si2Mn steel substrate and FeCrV15 alloy coatings. The microstructure FeCrV15 alloy coating consists of γ-Fe, V_8C_7, and Cr_7C_3.
2. The microhardness values of the coatings prepared at different scanning speeds were all higher than those of the substrate, with increasing values as the scanning speed increased. When the scanning speed was 8 mm/s, the maximum microhardness reached 727.5 ± 27 HV, approximately 2.5 times that of the substrate.
3. The average coefficients of friction of the coatings prepared at different scanning speeds were all lower than that of the substrate, with a decrease in average coefficients of friction as the scanning speed increased. At a scanning speed of 8 mm/s, the coating exhibited the best wear resistance. The main wear mechanisms of the coating are oxidative wear and adhesive wear, with a small amount of abrasive wear.

Author Contributions: Investigation, Z.B.; Writing—original draft, Z.B.; Supervision, T.L.; Writing—review and editing, T.L. All authors have read and agreed to the published version of the manuscript.

Funding: National Natural Science Foundation of China (Grant No. 51605201).

Data Availability Statement: The original contributions presented in the study are included in the article; further inquiries can be directed to the corresponding authors.

Acknowledgments: Thanks for Yongjie Wan's help in laser cladding experiment.

Conflicts of Interest: The authors declare no conflicts of interest.

References

1. Kalácska, Á.; De Baets, P.; Fauconnier, D.; Schramm, F.; Frerichs, L.; Sukumaran, J. Abrasive Wear Behaviour of 27MnB5 Steel Used in Agricultural Tines. *Wear* **2020**, *442–443*, 203107. [CrossRef]
2. Guul-Simonsen, F.; Jørgensen, M.H.; Have, H.; Håkansson, I. Studies of Plough Design and Ploughing Relevant to Conditions in Northern Europe. *Acta Agric. Scand. B Soil. Plant Sci.* **2002**, *52*, 57–77. [CrossRef]
3. Wu, T.; Shi, W.; Xie, L.; Gong, M.; Huang, J.; Xie, Y.; He, K. Study on the Effect of Ni60 Transition Coating on Microstructure and Mechanical Properties of Fe/WC Composite Coating by Laser Cladding. *Opt. Laser Technol.* **2023**, *163*, 109387. [CrossRef]
4. Monção, F.C.; Caliari, F.R.; Freitas, F.E.; Couto, A.A.; Augusto, A.; Lima, C.R.C.; Massi, M. Wear Resistance Evaluation of Self-Fluxing Nickel-Based Coating Deposited on AISI 4340 Steel by Atmospheric Plasma Spray. *Metals* **2024**, *14*, 532. [CrossRef]
5. Kucharska, B.; Bochra, K.; Wierzchoń, T.; Sobiecki, J.R. Protective Magnetron Sputtering Physical Vapor Deposition Coatings for Space Application. *Coatings* **2024**, *14*, 1195. [CrossRef]
6. Günther, K.; Bergmann, J.P. Influencing Microstructure of Vanadium Carbide Reinforced FeCrVC Hardfacing during Gas Metal Arc Welding. *Metals* **2020**, *10*, 1345. [CrossRef]
7. Cao, Z.; Liu, T.; Yu, F.; Cao, W.; Zhang, X.; Weng, Y. Carburization Induced Extra-Long Rolling Contact Fatigue Life of High Carbon Bearing Steel. *Int. J. Fatigue* **2020**, *131*, 105351. [CrossRef]
8. Guardian-Tapia, R.; Rosales-Cadena, I.; Roman-Zubillaga, J.L.; Gonzaga-Segura, S.R. Mechanical and Microstructural Characterization of AISI 316L Stainless Steel Superficially Modified by Solid Nitriding Technique. *Coatings* **2024**, *14*, 1167. [CrossRef]
9. Wang, C.; Yan, X.; Zhang, T.; Zhang, Q.; Zhang, Z. Microstructure and Tribological Properties of WC/Ni-MoS2 Titanium-Based Composite Coating on TC4. *Coatings* **2024**, *14*, 1157. [CrossRef]
10. Liu, C.; Li, C.; Zhang, Z.; Sun, S.; Zeng, M.; Wang, F.; Guo, Y.; Wang, J. Modeling of Thermal Behavior and Microstructure Evolution during Laser Cladding of AlSi10Mg Alloys. *Opt. Laser Technol.* **2020**, *123*, 105926. [CrossRef]
11. Erfanmanesh, M.; Shoja-Razavi, R.; Abdollah-Pour, H.; Mohammadian-Semnani, H.; Barekat, M.; Hashemi, S.H. Friction and Wear Behavior of Laser Cladded WC-Co and Ni/WC-Co Deposits at High Temperature. *Int. J. Refract. Metals Hard Mater.* **2019**, *81*, 137–148. [CrossRef]
12. Gao, S.; Fu, Q.; Li, M.; Huang, L.; Liu, N.; Cui, C.; Yang, B.; Zhang, G. Optimization of Laser Cladding Parameters for High-Entropy Alloy-Reinforced 316L Stainless-Steel via Grey Relational Analysis. *Coatings* **2024**, *14*, 1103. [CrossRef]
13. Ma, S.; Zhang, C.; Li, L.; Chen, H.; Yang, Y. Effects of Tungsten Addition on the Microstructure and Properties of FeCoCrNiAl High-Entropy Alloy Coatings Fabricated via Laser Cladding. *Materials* **2024**, *17*, 3592. [CrossRef] [PubMed]
14. Bartkowski, D.; Bartkowska, A. Wear Resistance in the Soil of Stellite-6/WC Coatings Produced Using Laser Cladding Method. *Int. J. Refract. Metals Hard Mater.* **2017**, *64*, 20–26. [CrossRef]
15. Hou, X.; Du, D.; Wang, K.; Hong, Y.; Chang, B. Microstructure and Wear Resistance of Fe-Cr-Mo-Co-C-B Amorphous Composite Coatings Synthesized by Laser Cladding. *Metals* **2018**, *8*, 622. [CrossRef]

16. Lu, J.Z.; Cao, J.; Lu, H.F.; Zhang, L.Y.; Luo, K.Y. Wear Properties and Microstructural Analyses of Fe-Based Coatings with Various WC Contents on H13 Die Steel by Laser Cladding. *Surf. Coat. Technol.* **2019**, *369*, 228–237. [CrossRef]
17. Aramide, B.; Pityana, S.; Jamiru, T.; Popoola, P.; Sadiku, R. Influence of Vanadium-Chromium Carbide on the Microstructure of Reinforced FeCrV15 Hardfacing during Laser Cladding Deposit. *J. Mater. Eng. Perform.* **2022**, *31*, 514–523. [CrossRef]
18. Aramide, B.; Popoola, P.; Sadiku, R.; Jamiru, T.; Pityana, S. Influence of Extra Chromium Addition on the Microstructure, Hardness, and Corrosion Behaviour of High Carbon Ferrochrome FeCrV15 Deposited through Laser Cladding on Steel Baseplate for Tillage Application. *Surf. Topogr.* **2021**, *9*, 045029. [CrossRef]
19. Blau, P.J. On the Nature of Running-In. *Tribol. Int.* **2005**, *38*, 1007–1012. [CrossRef]
20. Liang, Y.; Fu, H.; Xing, Z.; Guo, X.; Lin, J. Effect of Cr_3C_2 Content on Microstructure and Properties of Laser Cladding Ti(C, B)/Ni Coatings. *J. Mater. Eng. Perform.* **2022**, *31*, 5189–5200. [CrossRef]